JOURNAL OF AEROSPACE COMPUTING, INFORMATION, AND COMMUNICATION
Vol. 4, May 2007

Towards Vision-Based Autonomous Landing for Small UAVs – First Experimental Results of the Vision System

H.-W. Schulz,* M. Buschmann,† L. Krüger,‡ S. Winkler,§ and P. Vörsmann**
Institute of Aerospace Systems, Technical University of Braunschweig, Braunschweig, 38108, Germany

This paper describes the current development of intelligent vision capabilities for small sized Unmanned Aerial Vehicles (UAV) as part of the program "CAROLO" at the Technical University of Braunschweig, Germany. The objective of this development is to create image processing algorithms and appropriate hardware that suits the requirements of small sized UAVs. Enabling vision-based flight guidance during landing was chosen as the first task and acts as a technology demonstrator for future vision capabilities. The characteristics of a laid out marker are extracted from the on-board imagery. Relative position and attitude of this marker relative to the body-fixed coordinate system are determined. This concept conveys information about the designated landing point to the aircraft. An experimental installation of the vision system was used for first measurements. This experiment and its results – in particular the attainable accuracies of the presented vision system, are the subject of this publication.

Nomenclature

$_c$	subscript for camera coordinate system
$_m$	subscript for marker coordinate system
^{M}	superscript for the marker
$\underline{\underline{H}}^{cm}$	homography matrix
$\underline{\underline{K}}$	camera calibration matrix
$\underline{\underline{R}}$	rotation matrix
$\underline{\underline{T}}^{cm\prime}$	transformation matrix (before scaling)
$\underline{\underline{T}}^{cm}$	transformation matrix (after scaling)
c_x, c_y	camera principal point
d	distance
f	focal length
h	components of the homography matrix
r	components of the rotation matrix
$\underline{t}$	translation vector
t	components of the translation vector
u, v	coordinates of the marker points (2-D)

Presented as paper 2005-6980 at the Infotech@Aerospace 2005 Conference and Exhibit, Arlington, Virginia, 26 September 2005; received 26 July 2006; revision received 31 January 2007; accepted for publication 19 February 2007.

* Research Associate, Dr.-Ing. candidate, ha.schulz@tu-bs.de, AIAA Member
† Research Associate, Dr.-Ing. candidate, m.buschmann@tu-bs.de
‡ Research Associate, Dr.-Ing. candidate, lars.krueger@tu-bs.de
§ Research Associate, Dr.-Ing. candidate, s.winkler@tu-bs.de
** Head of Institute, Prof. Dr.-Ing., p.voersmann@tu-bs.de, AIAA Member

x, y, z	coordinates of the marker points (3-D)
x^M, y^M, z^M	coordinates of the marker
Φ, Θ, Ψ	Euler angles
λ	scale factor

I. The Motivation

IN 2001 "a completely autonomous micro aerial vehicle with dimensions as small as possible" was defined to be the goal of the research project "CAROLO" of the Institute of Aerospace Systems at the Technical University of Braunschweig. This goal was achieved in 2004: "CAROLO P50", an aircraft with 50 cm wing span only and 540 g take-off mass, takes off independently, flies autonomously along predefined waypoints and sends video to the ground. Landing the aircraft at a predefined point is completely autonomous as well. Details about all unmanned aircraft of the CAROLO family and the on-board navigation system can be found in.[1]

Interest in micro and mini aerial vehicles is increasing not only from the research community but prospective users as well. Despite the advantages that autonomy brings already, the mission-specific abilities of these small aircraft can and must be extended further. A next step of research shall now introduce image-processing abilities to mini and small UAVs.

In the field of UAVs, image processing is used either for navigation or as part of the payload. The latter is currently rarely found in small UAVs, but a good example is establishing the relative position of a target from a video signal received on the ground and sending it back to the aircraft for camera control.[2] More commonly, vision-based systems are used to extract horizon information,[3,4] to support landings[5–9] or – with increasing importance – to act as a sense & avoid system.[10] Two approaches have to be distinguished: Image processing is either done on the ground and information is sent back to the aircraft or the task is addressed by on-board hardware. However, in most cases where image processing is done on-board, mass, dimensions and power consumption of the current systems prohibit the use of this hardware on board distinctively smaller UAVs. In summary it can be stated, that there is a lack of capabilities below the unmanned aircraft which are big enough to use currently available image processing hardware on board. This cannot be changed by doing the image processing on the ground because this would decrease range and safety. The goal has to be on-board image processing. It does not only represent a challenge, but contributes to an increased usefulness of these aircraft.

A computer system with appropriate computing power, which fulfills the special requirements of mini aerial vehicles regarding mass, space, and power consumption, is currently under development at the Institute of Aerospace Systems (Fig. 1). The camera offers a resolution of 1024×768 Pixel^2 at a weight of 50 g. The high quality lens has an aperture angle of 60° and weighs 120 g. Lighter lenses are available but generally produce more lens distortion.

Fig. 1 On-board image processing system for small UAVs; foreground: image processing unit; background: aluminum frame, downward facing camera lens; backside (not visible): camera, power supply, CAROLO on-board navigation computer.

Future tests have to verify if this could be accepted. With 64 g for the image processing unit and 25 g for the CAROLO navigation computer the resulting image processing system is well suited for mini and small UAVs.

In order to demonstrate the extended abilities during flight, the following goal was defined: Information extracted from image data of an on-board camera shall support the flight guidance of the UAV during approach. Thus, the camera acts as an additional sensor. In contrast to the autonomous take-off of a small UAV, landing proves to be more difficult. Direct measurement of altitude above ground is not possible using the sensors that are typically available on board small UAVs. The sensors might include GPS (Global Positioning System), IMU (Inertial Measurement Unit), and barometric altimeter. However, for a precise landing the altitude above ground is an indispensable variable. Determining altitude above ground from the altitude of the earth's surface and the absolute altitude of the aircraft is problematic as well: Reliable altitude data of the landing point might not be available and the vertical GPS-measurement is not accurate enough for determining the absolute altitude of the aircraft.

II. The Procedure

To tackle this problem, a known marker – indicating the preferred landing point – shall be recognized by an onboard camera and its position shall be determined. The system will be implemented in the fully autonomous mini UAV "CAROLO T200" depicted in Fig. 2, which offers 2 kg payload at 4 kg MTOW and 2 m wingspan. Aircraft of this category often land directly on the fuselage without need for a landing gear and then come to a halt within less than 5 m. Assuming that the landing field is reasonably flat and level, it seems sufficient to specify a landing point rather than a landing area. To match the high mobility of mini and small UAV systems, the marker is made of synthetic canvas cover which is clamped to a foldable frame. This provides a lightweight but dimensionally stable marker which can be easily laid out at the desired landing point by the UAV's operator.

Ideally, the camera used to determine the altitude above the landing point will be the same camera used for surveillance during the aircrafts mission. Most of these cameras are downward facing cameras. The landing procedure and the image processing algorithms have to take this into account. With a downward facing camera the marker will be in the field of view of the camera for a short period of time only. That is why, contrary to other current approaches which use an on-board camera and visual ground aids, the marker does not have to be in view constantly. Theoretically, one measurement is sufficient to determine the navigation solution. Nevertheless, the flight path prior to landing is planned in a way that the aircraft passes the marker several times. Starting at a higher altitude – where the field of view is larger – the UAV will fly over the assumed landing point position. Using the measurements of the first pass, a new flight path can be calculated to pass the marker at a lower altitude, providing even better measurements. Simulation results show that three passes at 60, 45 and 30 meters will be sufficient for a safe landing. An example of the modular flight path is shown in Fig. 3.

Extensive research has been focused on aircraft state estimation which is especially important during approach and landing. An integrated navigation system, including GPS and a MEMS[#]-based IMU, was developed and successfully tested at the Institute of Aerospace Systems.[11] Even though determination of absolute altitude using GPS is still error-prone, good results for capturing changes in altitude could be achieved. The authors are confident that – given a vision based reference altitude above the landing point and using the integrated navigation system – a precise landing can be achieved.

Fig. 2 CAROLO T200 (pictured here with wind measuring 9-hole-probe and other meteorological sensors).

[#]MEMS - micro electro mechanical system

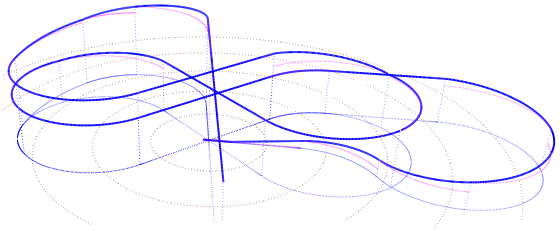

Fig. 3 Simulated, exemplary flight path towards the landing point (center); allows for three more passes to increase accuracy and reliability of vision measurements.

The vision algorithms used, the experimental setup and first ground based experimental results are presented in the following chapters.

III. The Algorithms

A passive optical measurement extracts fixed characteristics from a known object (Fig. 4) to determine position and attitude relative to this object. A similar procedure as the one described here has already been used in,[12] but an implementation was restricted to camera-to-target ranges of around 70 cm only. Relevant changes were made to the correction of camera distortion and the algorithms for marker identification. Some optimizations were made with special features of the future computer system in mind.

The mapping of a planar object onto the image plane of a camera is a perspective transformation. The general transformation of a point from the original plane (subscript m) onto the image or camera plane (subscript c) can be described in homogeneous coordinates as follows:

$$\begin{bmatrix} u_c \\ v_c \\ 1 \end{bmatrix} \sim \underline{\underline{H}}^{cm} \begin{bmatrix} u_m \\ v_m \\ 1 \end{bmatrix} = \begin{bmatrix} h_{11} & h_{12} & h_{13} \\ h_{21} & h_{22} & h_{23} \\ h_{31} & h_{32} & h_{33} \end{bmatrix} \begin{bmatrix} u_m \\ v_m \\ 1 \end{bmatrix} \tag{1}$$

The matrix $\underline{\underline{H}}^{cm}$ is called the homography. The transformation at hand is a special case of two-dimensional geometry. For this special perspective transformation the following applies:

$$h_{33} = 1 \tag{2}$$

This results in two equations with 8 unknown variables h_{11} to h_{32}:

$$u_c \cdot (h_{31} \cdot u_m + h_{32} \cdot v_m + 1) = h_{11} \cdot u_m + h_{12} \cdot v_m + h_{13} \tag{3}$$

$$v_c \cdot (h_{31} \cdot u_m + h_{32} \cdot v_m + 1) = h_{21} \cdot u_m + h_{22} \cdot v_m + h_{23} \tag{4}$$

Thus, to determine the 8 unknown quantities 4 corresponding pairs of points must be known. These corresponding pairs must be assigned to each other unambiguously. The marker coordinates of each point u_m and v_m are known for

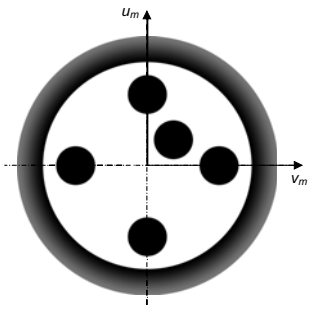

Fig. 4 Marker and marker coordinate system (subscript *m*).

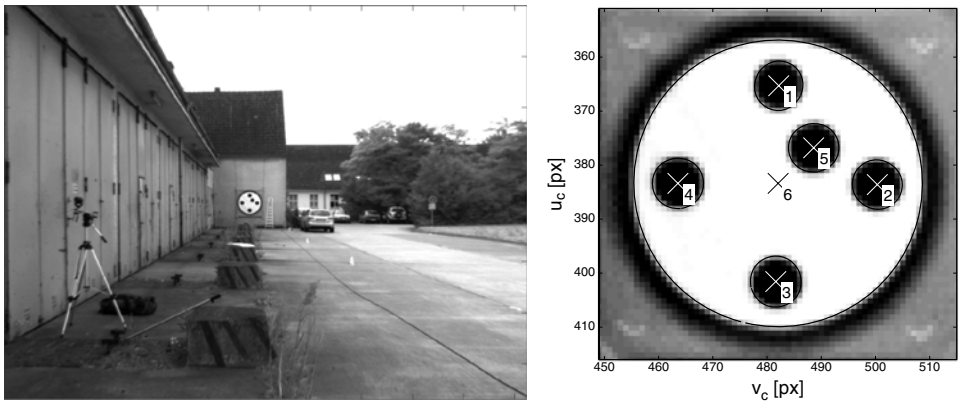

Fig. 5 Extracted marker (original image and magnification with ellipses and classification).

the fixed marker. These points are the centers of the four outer black circles. The fifth black circle is used to prevent rotation symmetry. Additionally, its center and the center of the outer (white) ellipse of the marker can be used to form an over-determined set of equations to determine the homography. This reduces error propagation. Additionally, the set of equations may be simplified by picking a particular coordinate system (Fig. 4).

To measure the coordinates u_c and v_c of the marker points in the image plane, methods of digital image processing are applied. These are:

1) detect the edges from the grayscale image with sub-pixel-accuracy[13]
2) capture the contours of all individual objects separately
3) correct the object contours (undo lens and camera distortion)[14]
4) fit ellipses to every individual contour[15]
5) classify the individual ellipses; identify the 6 points of the marker (ellipse centers)

These steps are fairly straightforward image processing algorithms except for step 3), where a different approach than usual was taken. Rather than undo lens distortion for the complete grayscale image, it is sufficient to undistort the object contours only, which saves a lot of computation. Therefore, the physical distortion model of the camera lens (radial and tangential distortion of 2nd order) must be inverted. This can be done with an approximation only. However, it can be shown that the resulting error is negligible.[14] After the five steps of image processing the coordinates u_c and v_c of the marker points are available and the homography $\underline{\underline{H}}^{cm}$ can be determined.

To compute position and attitude of the marker with respect to the aircraft body-fixed frame, the relationship between the two-dimensional camera fixed frame $[u_c; v_c]$ and the camera-fixed three-dimensional coordinate system $[x_c; y_c; z_c]$ has to be defined:

$$\begin{bmatrix} u_c \\ v_c \\ 1 \end{bmatrix} \sim \underline{\underline{K}} \begin{bmatrix} x_c \\ y_c \\ z_c \\ 1 \end{bmatrix} = \begin{bmatrix} f_x & 0 & c_x & 0 \\ 0 & f_y & c_y & 0 \\ 0 & 0 & 1 & 0 \end{bmatrix} \begin{bmatrix} x_c \\ y_c \\ z_c \\ 1 \end{bmatrix} \tag{5}$$

For the purpose of this early stage research, the aircraft body-fixed frame and the camera-fixed Cartesian coordinate system are assumed to be identical. They differ only by constant angles and positions, which may be accounted for at a later stage, when a real aircraft is used during test flights.

Equation (5) uses the so called intrinsic parameters focal length $[f_x; f_y]$ and principal point $[c_x; c_y]$, which can be determined as part of the camera calibration procedure.[16]

Finally, the sought-after transformation $\underline{\underline{T}}^{cm}$, describing the transformation from the marker frame to the camera-fixed (body-fixed) frame as a rotation $\underline{\underline{R}}$ and a translation $\underline{t}$, can be calculated as:

$$\begin{bmatrix} x_c \\ y_c \\ z_c \\ 1 \end{bmatrix} = \underline{\underline{T}}^{cm} \begin{bmatrix} u_m \\ v_m \\ 0 \\ 1 \end{bmatrix} = \begin{bmatrix} r_{11} & r_{12} & r_{13} & t_x \\ r_{21} & r_{22} & r_{23} & t_y \\ r_{31} & r_{32} & r_{33} & t_z \\ 0 & 0 & 0 & 1 \end{bmatrix} \begin{bmatrix} u_m \\ v_m \\ 0 \\ 1 \end{bmatrix} \tag{6}$$

Combining Eq. (1), (5) and (6) finally yields:

$$\underline{\underline{T}}^{cm\prime} = \begin{bmatrix} r_{11} & r_{12} & t_x \\ r_{21} & r_{22} & t_y \\ r_{31} & r_{32} & t_z \end{bmatrix} = \lambda \cdot \underline{\underline{K}}^{-1} \cdot \underline{\underline{H}}^{cm} \tag{7}$$

λ is a scaling factor, which can be determined using an additional constraint valid for rotation matrices: The norm of each row has to equal 1. After applying this constraint, the third column of the rotation matrix can be calculated using the cross product of the first two columns.

IV. The Experiment

In order to validate the algorithms, they were implemented onto commercially available PC hardware. The camera system used for this experiment is the same camera to be used in later flight tests. The camera was calibrated and the inverse camera calibration parameters were determined. The marker used for the measurements has a diameter of 2 m, which is expected to be sufficient for the envisioned landing procedure. To simplify the experiment, the overall setup has been rotated about 90° resulting in the camera axis being parallel to the earth's surface. This does not have any effect on the coordinate frames used or the performance of the algorithms. The camera-fixed Cartesian coordinate system is shown in Fig. 6.

To examine the performance of the presented algorithms, reference measurements of high accuracy must be conducted. An electronic tachymeter from the field of geodesy provided these measurements. A specially manufactured adapter was used so the instrument can be exchanged with the camera. The optical axes of camera and tachymeter were aligned to be identical using an additional measurement. Thus, the position of 4 corner points of the marker can be measured in the camera-fixed coordinate system (Fig. 7). With these measurements the attitude of the marker in the camera-fixed frame can be calculated as well as the position. The position of the single marker corner points can be determined within a few millimeters for the range of the examined distances. Thus, one receives a sufficiently accurate reference measurement.

For each data set consisting of 40 to 60 images – taken under completely identical conditions – one reference measurement was conducted. During the experiment position and orientation of the camera were varied, in order to examine the influence of different parameters. Thus nadir photographs from 20 m up to 60 m were taken. Additionally

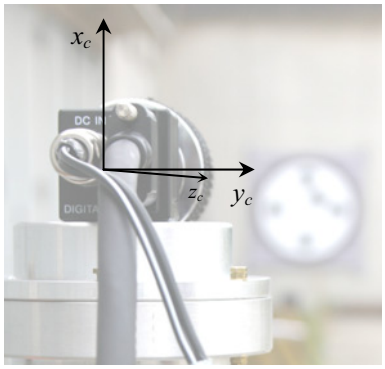

Fig. 6 Camera-fixed frame (subscript *c*).

Fig. 7 Experimental installation, camera on adapter, geodesy tachymeter, measuring the marker corner points.

the angle Φ^{cm} between marker and camera coordinate system was varied from 0° to 52° – resulting in a skewed view of the marker. Measurements were taken with the marker both in the center of the picture and at the edge, in order to analyze possible influences from camera distortion and distortion correction. Table 1 summarizes the conditions for all measurements done. Additionally, one can see, how many measurements (images) were taken for each of the 26 data sets.

Table 1 Summary of the measurements.

data set	**1**	**2**	**3**	**4**	**5**	**6**	**7**	**8**	**9**
quantity	50	50	50	60	40	40	40	40	40
distance	20 m	30 m	40 m	50 m	50 m	50 m	50 m	60 m	50 m
Φ^{cm}	0 °	0 °	0 °	0 °	3 °	10 °	20 °	0 °	30 °
camera axis	center	center	center	center	slightly right	right	extreme right	center	center
	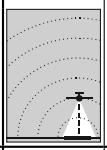	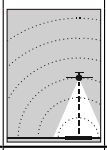	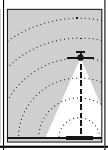	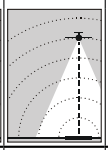	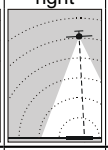	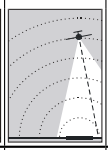	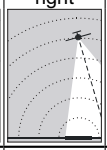	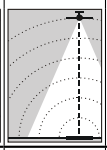	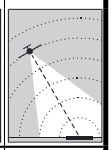
data set	**10**	**11**	**12**	**13**	**14**	**15**	**16**	**17**	**18**
quantity	40	40	40	40	40	40	40	40	40
distance	35 m	45 m	25 m	30 m	30 m	30 m	30 m	30 m	30 m
Φ^{cm}	0 °	0 °	25 °	5 °	10 °	20 °	30 °	50 °	0 °
camera axis	center	center	center	center	center	center	center	center	center
	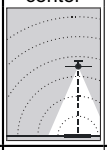	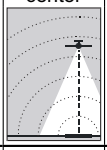	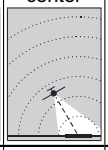	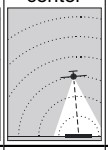	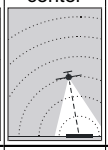	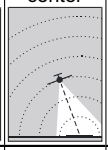	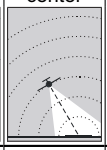	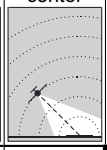	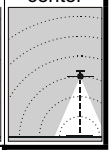
data set	**19**	**20**	**21**	**22**	**23**	**24**	**25**	**26**	
quantity	40	40	40	40	40	40	40	40	
distance	30 m	30 m	30 m	30 m	29 m	31 m	30 m	30 m	
Φ^{cm}	3 °	5 °	0 °	0 °	0 °	0 °	0 °	0 °	
camera axis	center	center	50cm left	50cm right	center	center	slightly left	left	
	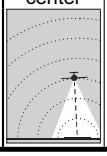	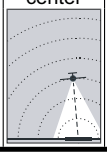	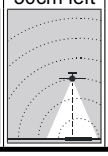	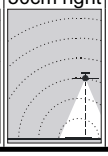	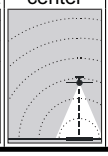	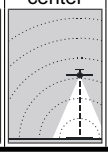	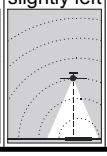	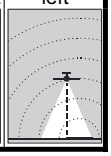	

V. The Results[‡‡]

In this section some results of the experiment will be presented. The images to each reference measurement do not differ at first sight. However, the image data contains noise, which affects the image processing and thus the determination of the homography $\underline{\underline{H}}^{cm}$ and the transformation matrix $\underline{\underline{T}}^{cm}$ as well.

Due to the flexibility of its material, the marker can dent slightly. This was observed during gusts of wind. However, the position of the marker characteristics (black circles on the marker) was affected only perpendicular to the marker plane so this didn't effect the measurement unless the marker was observed from a higher angle as seen in data set 17. In these cases the measured coordinates $[u_c; v_c]$ of the contours exhibit differences up to 0.4 pixels from one measurement to another. These movements of the marker material cannot be detected with the reference measurement.

The measured distance between marker and camera shall be analyzed first. This distance is calculated in the same way as the reference distance measurement:

$$d_c^M = \sqrt{x_c^{M^2} + y_c^{M^2} + z_c^{M^2}} \tag{8}$$

Fig. 8 shows the distribution of the 40 distance measurements $d_{c,Cam}^M$ of data set 23. Additionally, true value (reference measurement) and median value are shown. The difference between these two values for data set 23 is only 1 cm, which is an error of only 0.03%. But one can see that the measured values scatter. 90% of all measurements exhibit errors in the range of -0.35% to 0.24%. This is marked by the white range in Fig. 8. Bearing in mind, that data set 23 contains only 40 samples, no reliable statement can be made about the distribution of the samples, even though it might be described as normally distributed. It will be shown, that this is not true for measurements covering greater distances.

Since mean or median value do not represent the entire behavior of the data and thus the performance of the algorithms, evidence must be given about the distribution of the data depending on the varied parameters. For the remaining figures the so called boxplot[18] is used to achieve exactly that. Its advantages can be seen clearly in Fig. 11. The boxes contain 25% of the measured values above and 25% of the measured values below the median of the data set respectively (upper and lower quartiles). The median itself is represented in the box as well as a horizontal line. Measured values outside the box are indicated as whiskers. Outliers are classified as such, if they lie outside of 1.5 times the range of the upper and lower quartiles. Thus, the boxplot is suitable for the representation of the data at hand, which is not normally distributed. The big diagonal crosses additionally mark the value of the reference measurement, which serves as the true value. As "DS #" the numbers of the represented data sets are indicated. Fig. 9 depicts the distance measured by the camera against the true (reference) distance. It can be seen clearly, that the scatter of the measured values increases for distances of 50 m and more. Especially for 60 m the data does not scatter around the true value but around a significantly smaller value. Outliers as well are generally found below the true value. Especially the errors for the measurements with 60 m distance are significant. Errors up to 9 m can be seen and the median value for a measurement from 60 m distance is 4.2 m short of the true value. The reason for these characteristics will be discussed at a later point. Fig. 8 exhibits really small errors for data set 23 which was taken from around 30 m distance. Now Fig. 9 shows that these small errors can be found for all measurements from relatively short distances. Up to 45 m the achievable accuracy is quite astonishing. For a distance of 20 m the distance can be determined with an accuracy of 2 cm (the difference between upper and lower quartile is only 4 cm, centered on the true value).

The measurement of the distance $d_{c,Cam}^M$ with $\Phi_{Ref}^{cm} \approx 0°$ is mainly influenced by $z_{c,Cam}^M$. Analyzing $y_{c,Cam}^M$ (Fig. 10), it can be seen clearly, that the scatter does not increase until 60 m of distance. The small errors of the measurement are remarkable. All errors are in the range of 2 cm. Exhibiting very little scatter, the differences between median and true value might be errors in the alignment of camera and reference measurement instrument. However, this can not be proven.

[‡‡]The results presented here differ from the original publication[17] at the AIAA Infotech@Aerospace Conference 2005 in Arlington, VA. The improvements result from the new edge detection algorithm with now sub-pixel-accuracy, the inclusion of the fifth and sixth marker circle for determining the homography and finally a more robust method for calculating the Euler angles Φ, Θ and Ψ.

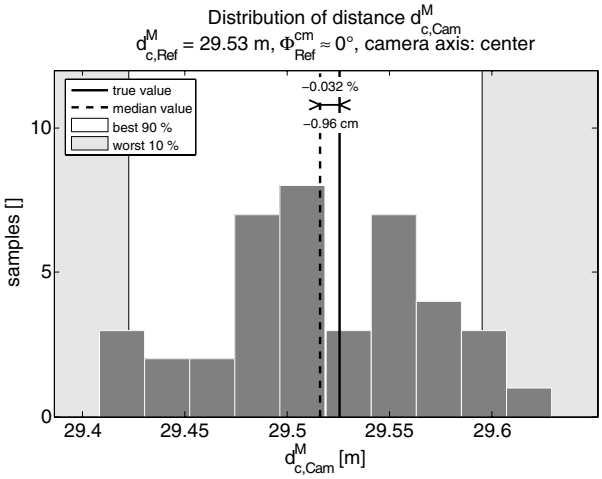

Fig. 8 Distribution of distance $d^{M}_{c,Cam}$, data set 23.

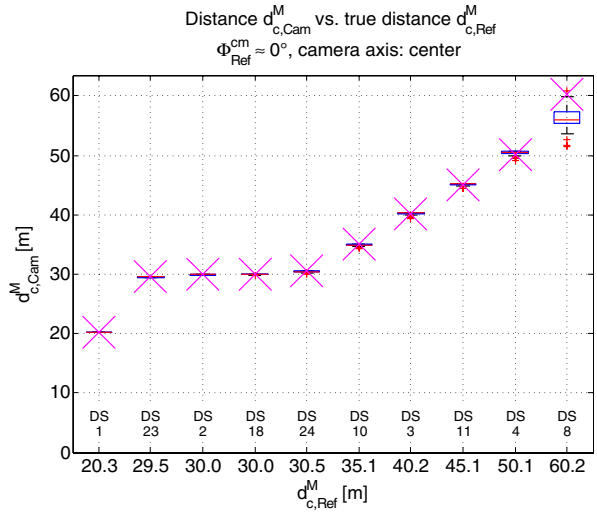

Fig. 9 Dependency on distance–distance $d^{M}_{c,Cam}$.

In Fig. 11 the bank angle Φ^{cm}_{Cam} is plotted against the increasing distance $d^{M}_{c,Cam}$. Scatter is strong and increases with distance. Errors up to 20° occur. This behavior had to be expected due to the geometry of the measurement, because a change in bank angle Φ^{cm}_{Cam} or pitch angle Ψ^{cm}_{Cam} results in minor changes of the marker image only. Therefore, it is difficult to detect.

The performance of the image processing algorithms shall be investigated for different bank angles, before more effort is put into explaining the origin of the mentioned errors. For this purpose, images of the marker were taken from different angles (variation of the bank angle Φ^{cm}_{Cam}). Fig. 12 shows the dependency of distance $d^{M}_{c,Cam}$ on bank angle Φ^{cm}_{Ref}. No increase in scatter or deviation of median value from true value with increasing bank angles can be seen. The errors are small compared to an increase in distance (Fig. 9). Based on a 30 m/0° measurement, an increase in distance of 20 m clearly produces larger errors than an increase in bank angle from 0° to 50°. Thus, assuming the optical resolution to be the limiting factor of the total system, the system must be designed primarily for the expected altitude during approach.

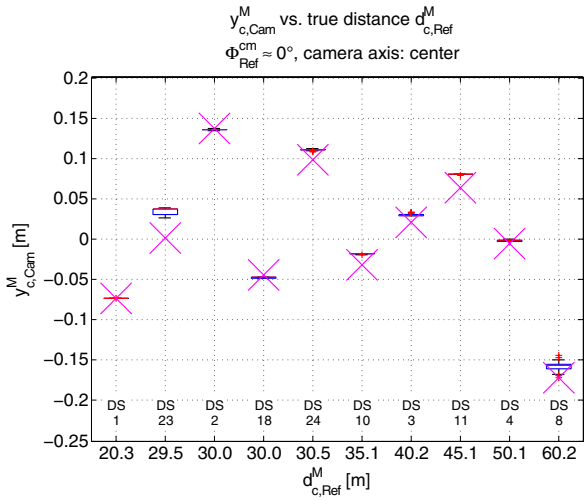

Fig. 10 Dependency on distance–distance $y^{M}_{c,Cam}$.

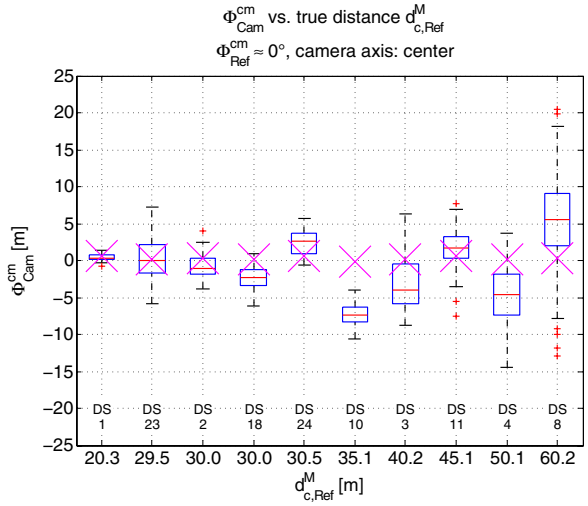

Fig. 11 Dependency on distance–angle Φ^{cm}_{Cam}.

Fig. 13 proves that the determination of the position perpendicular to the optical axis (z-axis) is not affected by varying bank angles. The achievable accuracy is remarkable.

Finally, Fig. 14 displays the measured bank angle Φ^{cm}_{Cam} against the true bank angle Φ^{cm}_{Ref}. Again, no significant deterioration over increasing bank angle can be observed.

In summary, increasing errors are mainly due to an increase in the distance between marker and camera. On closer examination of Eq. (1) it becomes clear, that errors in the coordinates u_c and v_c of every single marker point influence the homography matrix $\underline{\underline{H}}^{cm}$ directly. This matrix determines the transformation matrix $\underline{\underline{T}}^{cm}$ in Eq. (7):

$$\underline{\underline{T}}^{cm\prime} = \begin{bmatrix} r_{11} & r_{12} & t_x \\ r_{21} & r_{22} & t_y \\ r_{31} & r_{32} & t_z \end{bmatrix} = \lambda \cdot \underline{\underline{K}}^{-1} \cdot \underline{\underline{H}}^{cm} \tag{7}$$

As mentioned before, the scale factor λ must be calculated using an additional constraint for rotation matrices: The norm of all columns of the matrix must equal 1. Naturally, this must apply both to first and second column

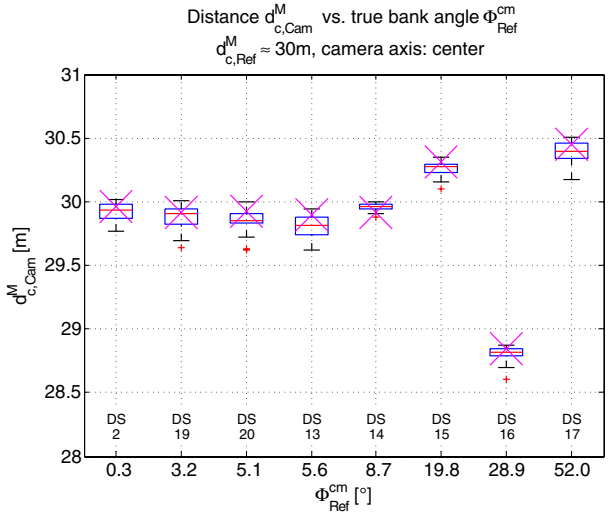

Fig. 12 Dependency on angle–distance $d^M_{c,Cam}$.

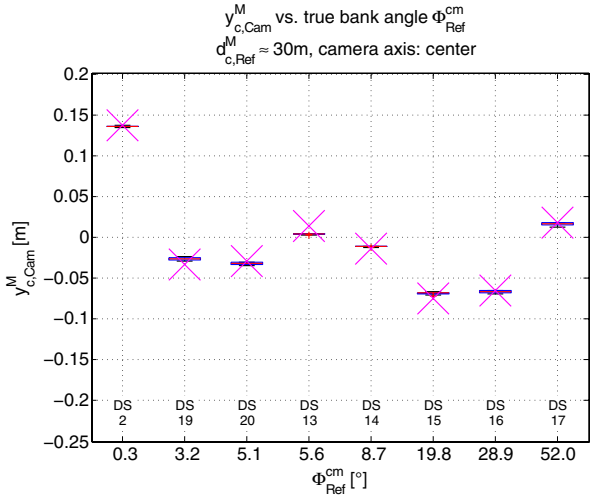

Fig. 13 Dependency on angle–distance $y^M_{c,Cam}$.

of $\underline{\underline{T}}^{cm\prime}$. However, errors in determining the image coordinates u_c and v_c of the corresponding marker points lead to an inconsistent homography $\underline{\underline{H}}^{cm}$, which in turn affects the calculation of r_{11} to r_{32}. Thus, the determination of the scale factor λ is error prone. Consequently, the resulting values of the translation vector $\underline{t}$ and the rotation matrix $\underline{\underline{R}}$ – being scaled using λ – will be affected by these errors. Originating from image processing errors, the errors in $\underline{t}$ and $\underline{\underline{R}}$ will increase with decreasing resolution of the marker circle contours, i.e. with increasing distance from camera to marker. This can be seen in Figures 9 to 14.

The computation of the third column of the rotation vector suffers from wrong scaling as well. The errors in r_{11} to r_{32} affect the newly calculated r_{13} to r_{33}. This seriously affects the presented algorithm, since the third column of the rotation matrix must be used to compute the angles Θ and Φ, which in turn affects the calculation of Ψ.

$$\underline{\underline{R}} = \begin{bmatrix} \cos\Theta\cos\Psi & \cos\Theta\sin\Psi & -\sin\Theta \\ \sin\Phi\sin\Theta\cos\Psi - \cos\Phi\sin\Psi & \sin\Phi\sin\Theta\sin\Psi + \cos\Phi\cos\Psi & \sin\Phi\cos\Theta \\ \cos\Phi\sin\Theta\cos\Psi + \sin\Phi\sin\Psi & \cos\Phi\sin\Theta\sin\Psi - \sin\Phi\cos\Psi & \cos\Phi\cos\Theta \end{bmatrix} \tag{9}$$

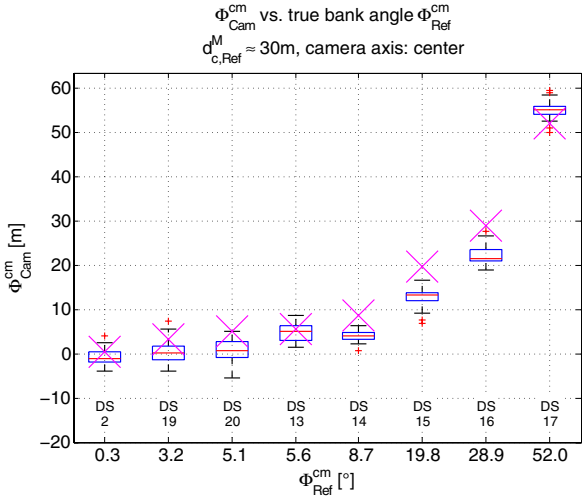

Fig. 14 Dependency on angle–angle Φ^{cm}_{Cam}.

To tackle these problems, the optical resolution of the marker must be high enough at any time. The following proposals could accomplish that:

1) restriction of maximum altitude (approx. 50 m for the presented overall system and a 2 m-marker)
2) decreasing camera aperture angle = increase in focal length (limits the observable area, marker might not be found)
3) increasing camera resolution (causes an increase in required computing power)
4) increasing marker size (degrades the handling of the otherwise highly mobile marker)

To demonstrate the feasibility of the proposed concept and to prove the performance of the intended image processing system a restriction to 50 m altitude is currently well acceptable.

VI. Conclusion and Outlook

A vision based method for determining relative position and attitude of a small, known marker was presented in this publication. Based on the experimental results and the hardware in use, it can be stated that the marker was identified reliably at any time and the vision based determination of relative position and attitude yields very good results for distances up to approximately 50 m. For other applications the maximum distance could be increased simply by using a bigger marker, since maximum distance and marker size are in direct proportion. Increasing the camera resolution or decreasing the camera aperture angle to extend the maximum distance is not recommended.

Simulation results have shown that the proposed landing procedure works well with the magnitude of errors encountered. Especially the high accuracy of both, lateral position of the landing point and heading for landing, reduces the necessary changes of the flight path once these quantities have been determined for the first time. Higher errors occur at higher altitudes but can be accepted due to the chosen multistage approach. The final pass over the marker produces highly accurate relative altitude measurements which are sufficient in order to land the unmanned aircraft precisely.

Using the extensive data base of the experiment in post processing, the image processing algorithms could be improved already. Current work is now directed at implementing the algorithms onto the on-board image processing computer. Its completion will be followed by integrating the computer and camera system into the test platform "CAROLO T200" for flight tests. The ultimate goal is the autonomous, vision based landing.

Acknowledgment

We would like to thank Bernd Hartwig of HHK Datentechnik Braunschweig for providing geodetic equipment and for supporting the preparation of the reference measurements.

References

[1]Schulz, H.-W., Buschmann, M., Kordes, T., Krüger, L., Winkler. S, and Vörsmann, P., "The Autonomous Micro and Mini UAVs of the Carolo-Family," *Proceedings of the AIAA Infotech@Aerospace* 2005, AIAA, Arlington, VA, Sep. 2005, Paper 2005-7092.

[2]Quigley, M., Goodrich, M. A., Griffiths, S., Eldredge, A., and Beard, R., "Target Acquisition, Localization, and Surveillance using a Fixed-Wing Mini-UAV and Gimbaled Camera," *Proceedings of the IEEE International Conference on Robotics and Automation (ICRA)*, IEEE, Barcelona, Spain, April 2005.

[3]Ettinger, S., Nechyba, M., Ifju, P., and Waszak, M., "Vision-Guided Flight Stability and Control for Micro Air Vehicles," *Proceedings of the IEEE International Conference on Intelligent Robots and Systems (IROS)*, IEEE, Lausanne, Switzerland, Sep. 2002.

[4]Cornall, T., and Egan, G., "Measuring Horizon Angle from Video on a Small Unmanned Air Vehicle," *Proceedings of International Conference on Autonomous Robots and Agents (ICARA)*, Palmeston, New Zealand, Dec. 2004.

[5]Petruszka, A., and Stentz, A., "Stereo vision automatic landing of VTOL UAVS," *Proceedings of the 23rd Annual Association for Unmanned Vehicle Systems International Symposium and Exhibition*, Orlando, FL, July 1996, pages 245–63.

[6]Yang, Z. F., and Tsai, W. H., "Using parallel line information for vision-based landmark location estimation and an application to automatic helicopter landing," *Robotics and Computer-Integrated Manufacturing*, Vol. 14, No. 4, pp. 297–306, Aug. 1998.

[7]Shakernia, O., Ma, Y., Koo, T.J., Hespanha, J., and Sastry, S., "Vision guided landing of an unmanned air vehicle," *Proceedings of the 38th IEEE Conference on Decision and Control*, IEEE, Phoenix, AZ, 1999, Vol. 4, pp. 4143–4148.

[8]Sharp, C. S., Shakernia, O., and Sastry, S. S., "A Vision System for Landing an Unmanned Aerial Vehicle," *Proceedings of the 2001 IEEE International Conference on Robotics and Automation*, IEEE, Seoul, Korea, May 2001, pp. 1720–1727.

[9]Saripalli, S., Montgomery, J. F., and Sukhatme, G. S., "Vision-based autonomous landing of an unmanned aerial vehicle," *Proceedings of the 2002 IEEE International Conference on Robotics and Automation*, IEEE, Washington, DC, May 2002, pp. 2799–2804.

[10]Thielecke, F., Dittrich, J., and Bernatz, A., "ARTIS–Ein VTOL UAV Demonstrator," *Proceedings of the Deutscher Luft- und Raumfahrtkongress 2004*, DGLR, Dresden, Germany, Sep. 2004, DGLR-JT2004-024.

[11]Winkler, S., "Zur Sensordatenfusion für integrierte Navigationssysteme unbemannter Kleinstflugzeuge (Sensor Data Fusion with Integrated Navigation Systems for Small Unmanned Aircraft)," *Doctoral Thesis at the Institute of Aerospace Systems at the Technical University of Braunschweig*, Faculty of Mechanical Engineering, Braunschweig, Germany, Feb. 2007.

[12]Schlaile, Ch., et al., "Stabilizing a Four-Rotor Helicopter using Computer Vision," *1st European Micro Aerial Vehicle Conference (EMAV)*, Braunschweig, Germany, 2004.

[13]Canny, J., "A Computational Approach to Edge Detection," *Transactions on Pattern Analysis and Machine Intelligence,* IEEE, Vol. 8, Nov. 1986, pp. 679–698.

[14]Heikkilä, J., and Silvn, O., "A Four-Step Camera Calibration Procedure with Implicit Image Correction," *Computer Society Conference on Computer Vision and Pattern Recognition,*IEEE, San Juan, Puerto Rico, 1997, pp. 1106–1112.

[15]Halíř, R., "Robust Bias-Corrected Least Squares Fitting of Ellipses," *8th International Conference in Central Europe on Computer Graphics, Visualization and Interactive Digital Media,* Plzen, Czech Republic, 2000.

[16]Heikkilä, J., "Calibration Toolbox for MATLAB," Version 3.0, http://www.ee.oulu.fi/∼jth/calibr/.

[17]Schulz, H.-W., Buschmann, M., Krüger, L., Winkler. S., and Vörsmann, P., "Vision-Based Autonomous Landing for Small UAVs – First Experimental Results," *Proceedings of the AIAA Infotech@Aerospace* 2005, AIAA, Arlington, VA, Sep. 2005, Paper 2005–6980.

[18]McGill, R., Tukey, J. W., and Larsen, W. A., "Variations of Boxplots," *The American Statistician*, Vol. 32, 1978, pp. 12–16.

Lyle Long
Associate Editor